

# Keck Observations Confirm a Super-Jupiter Planet Orbiting M-dwarf OGLE-2005-BLG-071L

David P. Bennett<sup>1,2</sup>, Aparna Bhattacharya<sup>1,2</sup>, Jean-Philippe Beaulieu<sup>3,4</sup>, Joshua W. Blackman<sup>3</sup>,  
Aikaterini Vandenrou<sup>3</sup>, Sean K. Terry<sup>5</sup>, Andrew A. Cole<sup>3</sup>, Calen B. Henderson<sup>6</sup>,  
Naoki Koshimoto<sup>1,2,7</sup>, Jessica R. Lu<sup>8</sup>, Jean Baptiste Marquette<sup>9</sup>, Andrzej Udalski<sup>10</sup>

<sup>1</sup>*Code 667, NASA Goddard Space Flight Center, Greenbelt, MD 20771, USA;*  
*Email: bennettd@umd.edu*

<sup>2</sup>*Department of Astronomy, University of Maryland, College Park, MD 20742, USA*

<sup>3</sup>*School of Physical Sciences, University of Tasmania, Private Bag 37 Hobart, Tasmania 7001  
Australia*

<sup>4</sup>*Institut d'Astrophysique de Paris, 98 bis bd Arago, 75014 Paris, France*

<sup>5</sup>*Department of Physics, Catholic University of America, 620 Michigan Ave., N.E. Washington,  
DC 20064, USA*

<sup>6</sup>*NASA Exoplanet Science Institute, IPAC/Caltech, Pasadena, California 91125, USA*

<sup>7</sup>*Department of Astronomy, Graduate School of Science, The University of Tokyo, 7-3-1 Hongo,  
Bunkyo-ku, Tokyo 113-0033, Japan*

<sup>8</sup>*University of California Berkeley, Berkeley, CA*

<sup>9</sup>*Laboratoire d'astrophysique de Bordeaux, Univ. Bordeaux, CNRS, B18N, alle Geoffroy  
Saint-Hilaire, 33615 Pessac, France*

<sup>10</sup>*Astronomical Observatory, University of Warsaw, Al. Ujazdowskie 4, 00-478 Warszawa, Poland*

## ABSTRACT

We present adaptive optics imaging from the NIRC2 instrument on the Keck-2 telescope that resolves the exoplanet host (and lens) star as it separates from the brighter source star. These observations yield the  $K$ -band brightness of the lens and planetary host star, as well as the lens-source relative proper motion,  $\mu_{\text{rel,H}}$  in the heliocentric reference frame. The  $\mu_{\text{rel,H}}$  measurement allows determination of the microlensing parallax vector,  $\pi_E$ , which had only a single component determined by the microlensing light curve. The combined measurements of  $\mu_{\text{rel,H}}$  and  $K_L$  provide the masses of the host star,  $M_{\text{host}} = 0.426 \pm 0.037 M_{\odot}$ , and planet,  $m_p = 3.27 \pm 0.32 M_{\text{Jupiter}}$  with a projected separation of  $3.4 \pm 0.5$  AU. This confirms the tentative conclusion of a previous paper (Dong et al. 2009b) that this super-Jupiter mass planet, OGLE-2005-BLG-071Lb,

orbits an M-dwarf. Such planets are predicted to be rare by the core accretion theory and have been difficult to find with other methods, but there are two such planets with firm mass measurements from microlensing, and an additional 11 planetary microlens events with host mass estimates  $< 0.5M_{\odot}$  and planet mass estimates  $> 2$  Jupiter masses that could be confirmed by high angular follow-up observations. We also point out that OGLE-2005-BLG-071L has separated far enough from its host star that it should be possible to measure the host star metallicity with spectra from a high angular resolution telescope such as Keck, the VLT, the Hubble Space Telescope or the James Webb Space Telescope.

*Subject headings:* gravitational lensing: micro, planetary systems

## 1. Introduction

The second exoplanet found by the microlensing method was OGLE-2005-BLG-071Lb, but the discovery paper did not do a detailed analysis of the higher order microlensing effects that could constrain the masses and distance of the lens system (Udalski et al. 2005). A more detailed analysis was done in a follow-up paper (Dong et al. 2009b) that included high angular resolution Hubble Space Telescope (HST) observations. Unfortunately, the light curve had no significant signal for finite source effects, and the HST observations were taken too soon after the event to get a strong measurement of the lens-source relative proper motion,  $\mu_{\text{rel}}$ . Furthermore, the light curve only constrains one component of the two-dimensional microlensing parallax vector,  $\pi_E$ , and the light curve measurements of  $\pi_E$ ,  $\mu_{\text{rel}}$ , were marginally inconsistent with each other. Finally, Dong et al. (2009b) pointed out that their estimates of the lens system masses and distance were dependent on the assumption that the excess flux seen at the location of the source in the HST images was due to the lens star, rather than a companion to the source. Nevertheless, with the assumption that the excess flux was due to the lens and planetary host star, they concluded that OGLE-2005-BLG-071Lb may be the most massive planet known to orbit an M-dwarf at the time of its publication in 2009.

In this paper, we use adaptive optics observations with the NIRC2 instrument on the Keck-2 telescope to identify the lens and planetary host star and provide a precise measurement of the masses and distance of the OGLE-2005-BLG-071L planetary system. These new results largely confirm the more tentative conclusions of Dong et al. (2009b), except for the conclusion that the lens system has thick disk kinematics.

Despite the decade between the publication of Dong et al. (2009b) and this paper, there are still very few known massive planets in wide orbits around low-mass stars. NASA’s exoplanet archive<sup>1</sup> lists only 19 planets with masses  $> 2M_{\text{Jupiter}}$  with semi-major between the snow line (taken to

---

<sup>1</sup><https://exoplanetarchive.ipac.caltech.edu/>

be at  $2.7(M/M_\odot)$  AU) and 30 AU orbiting stars main sequence stars with  $0.08M_\odot \leq M \leq 0.5M_\odot$  (Kennedy & Kenyon 2008). However, two of these are actually planets found by radial velocities with apparent typographical errors in the host masses, so that the correct masses are above  $0.5M_\odot$ . The only remaining planet found by radial velocities in this category is GJ 317 b (Johnson et al. 2007), which has host and planet masses of  $M_{\text{host}} = 0.42 \pm 0.05M_\odot$  and  $m_p = 2.5_{-0.4}^{+0.7}M_{\text{Jupiter}}$  with a semi-major axis of  $a = 1.15 \pm 0.05$  AU, based on a combination of radial velocity and astrometric data (Anglada-Escudé et al. 2012). This implies an overlap between the planet’s semi-major axis and our estimated snow line position of  $d_{\text{snow}} = 2.7(M/M_\odot)$  AU =  $1.161 \pm 0.135$  AU.

The remaining 16 of these wide orbit planets with super-Jupiter mass planets listed in the NASA Exoplanet Archive have been found by microlensing. These may seem to challenge the core accretion theory expectation that super-Jupiter mass planets should be rare in orbits around low-mass stars (Laughlin et al. 2004), but we must be careful to distinguish between planet and host star mass measurements and Bayesian mass estimates based on the assumption that all stars are equally likely to host a planet of the measured mass ratio,  $q$ . Recent AO image analysis for events MOA-2007-BLG-400 (A. Bhattacharya et al., in preparation) and MOA-2012-BLG-220 (A. Vandenroux et al., in preparation) has indicated host masses much larger than the previous Bayesian analyses suggested, indicating that this prior assumption that all stars are equally likely to host gas giant planets may be flawed. Therefore, it is important to focus on events with mass measurements.

The first microlens exoplanet with a confirmed planet mass of  $> 2M_{\text{Jupiter}}$  orbiting a low-mass star with  $0.08M_\odot \leq M \leq 0.5M_\odot$  was OGLE-2012-BLG-0406 (Poleski et al. 2014), which has host and planet masses of  $M_{\text{host}} = 0.44 \pm 0.07M_\odot$  and  $m_p = 2.73 \pm 0.43M_{\text{Jupiter}}$  according to a detailed analysis by Tsapras et al. (2014). In this paper, we present the second such microlens planet, OGLE-2005-BLG-071Lb with host and planet masses of  $M_{\text{host}} = 0.431 \pm 0.034M_\odot$  and  $m_p = 3.37 \pm 0.30M_{\text{Jupiter}}$  at a projected separation of  $3.4 \pm 0.5$  AU. However, unlike OGLE-2012-BLG-0406Lb, the planet OGLE-2005-BLG-071Lb is included in the combined statistical sample of Suzuki et al. (2016), which means that it can much more easily be included in a statistical analysis of planet properties. In fact, there are three other events from the Suzuki et al. (2016) sample that are candidates for super-Jupiter mass planets orbiting low mass ( $< 0.5M_\odot$ ) stars and that should allow host and planet mass measurements from high angular resolution follow-up observations. These are OGLE-2008-BLG-355 (Koshimoto et al. 2014), MOA-2009-BLG-387 (Batista et al. 2011) and MOA-2011-BLG-322Lb (Shvartzvald et al. 2014). Another candidate super-Jupiter mass planet in the Suzuki et al. (2016) sample orbiting a low mass star is MOA-2012-BLG-006 (Poleski et al. 2017), but a mass measurement for this event would be quite difficult, because of its bright giant source star. In addition to these events in the Suzuki et al. (2016) sample, the following events are candidates for super-Jupiter planets orbiting low-mass stars: MOA-2010-BLG-73, OGLE-2013-BLG-0102, OGLE-2013-BLG-1761, OGLE-2015-BLG-0954, MOA-2016-BLG-227, OGLE-2016-BLG-0263, KMT-2016-BLG-1397, and KMT-2017-BLG-1038 (Street et al. 2013; Jung et al. 2015; Hirao et al. 2017; Shin et al. 2016; Bennett et al. 2017; Koshimoto et al. 2017b; Zang et al. 2018; Shin et al. 2019). Perhaps the most interesting candidate is OGLE-2018-BLG-1011 (Han

et al. 2019), which has two super-Jupiter planets with mass ratios of 0.015 and 0.0095 orbiting a star with an estimated mass of  $\sim 0.2M_{\odot}$ .

This paper is organized as follows. In Section 2, we describe the Keck high angular resolution follow-up observations and their analysis, and in Section 3, we discuss the measured lens-source relative proper motion and how it can be used to constrain the microlensing parallax and angular Einstein radius. In Section 4, we explain how we constrain the light curve modeling in order to sample the light curves that are consistent with the data, and then we present the lens system masses, separation and distance that are implied by the combined light curve and Keck follow-up data in Section 5. Finally, we discuss the implications of these results and present our conclusions in Section 6.

## 2. Keck Follow up Observations and Analysis

We observed the source and lens stars for microlensing event OGLE-2005-BLG-071 with the NIRC2 instrument on the Keck-2 telescope on May 28, 2019 as a part of our NASA Keck Key Strategic Mission Support program entitled “Development of the WFIRST Exoplanet Mass Measurement Method.” The observations were carried out using both the NIRC2 wide and narrow cameras, which employ  $1024 \times 1024$  pixels with image scales of 39.686 mas/pixel and 9.942 mas/pixel, respectively. All Keck images were taken using the Keck-2 laser guide star adaptive optics system. The wide images are used for photometric calibrations, and we used a co-add of 8 of 10 dithered, wide camera images in the  $K_S$  passband to calibrate to reprocessed images from the VVV survey (Minniti et al. 2010), which is calibrated to 2MASS (Carpenter 2001) following Beaulieu et al. (2018). (Two of these wide camera images were not used due to relatively poor image quality.) These wide camera images were flat field and dark current corrected using standard methods, and then stacked using the SWarp Astrometrics package (Bertin et al. 2002). The details of our methods are described in Batista et al. (2014). We used aperture photometry on these wide camera images the SExtractor code (Bertin & Arnouts 1996). These wide images were used to detect and match as many bright isolated stars as possible to our custom reduction (Beaulieu et al. 2016) of the calibrated VVV images. Once the wide camera images were calibrated, we calibrated the narrow camera images to the wide camera images. This procedure provided an overall calibration precision for the co-added narrow camera image of 0.06 magnitudes.

We took 40 dithered NIRC2 narrow camera images on the same night as the wide camera images, and the 23 best images were combined to make the image shown in Figures 1(a) and (b) after correcting for achromatic differential refraction (Yelda et al. 2010) and geometric distortion (Service et al. 2016). Chromatic differential refraction is negligible compared to our measurement uncertainties (Gubler & Tytler 1998), so we ignore it. The point spread function (PSF) full-width, half-max (FWHM) of this image is  $\approx 65$  mas. Because the source and candidate lens stars are separated by  $\sim 1$  FWHM, we must analyze the Keck data with a PSF fitting code to measure the astrometry and photometry of this 2-star system. Following Bhattacharya et al. (2018), we

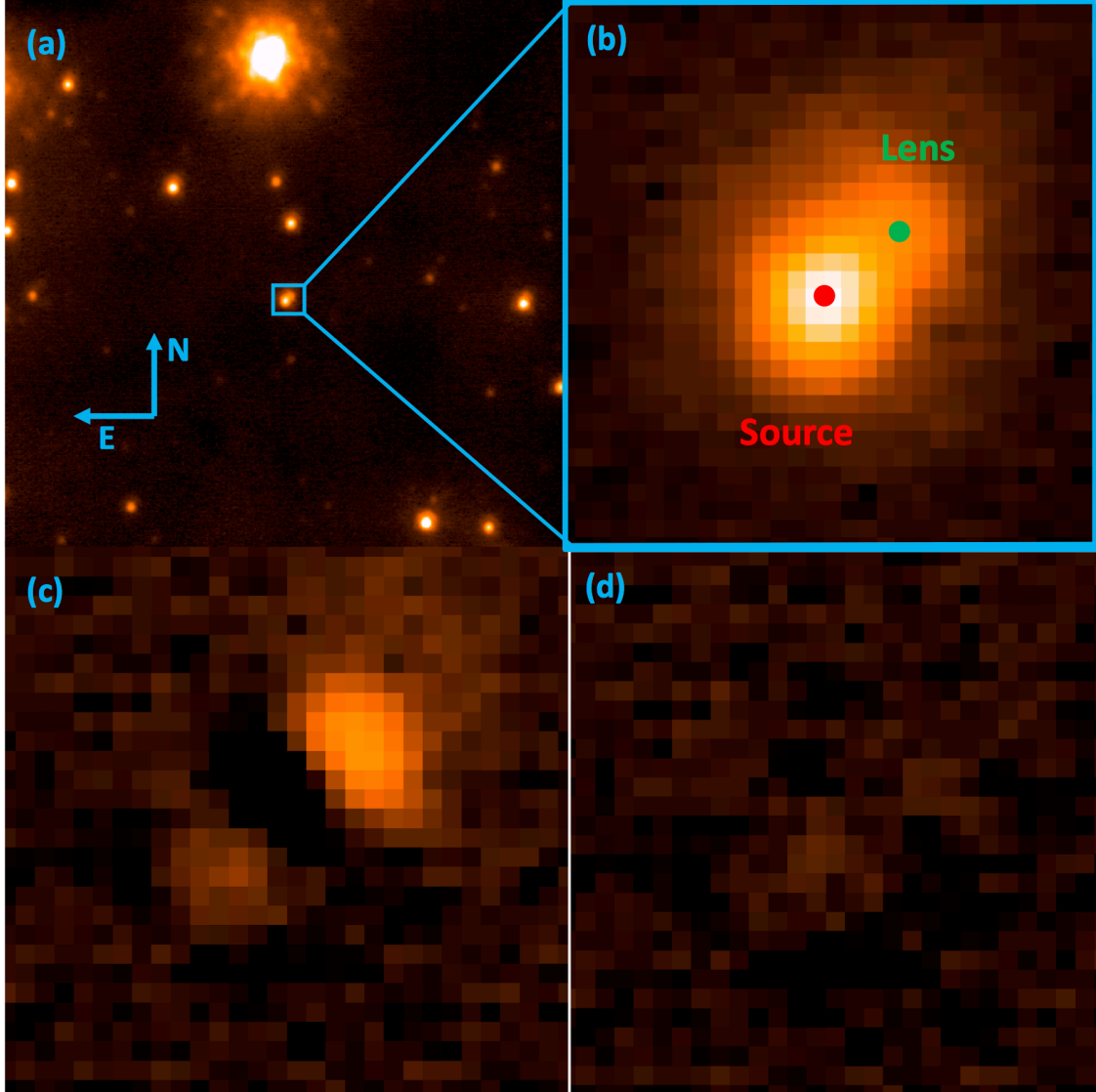


Fig. 1.— (a) The coadded sum of 23 60-sec exposure Keck-NIRC2 narrow camera images, and (b) a closeup of the OGLE-2005-BLG-071 source and lens stars on the right. The lens star is located  $41.5 \pm 1.3$  mas West and  $36.1 \pm 1.3$  mas North of the source star. (c) is the residual image from a DAOPHOT single star fit, and (d) is the residual image from a two-star fit.

use DAOPHOT (Stetson 1987) for this analysis, which has a proven ability to handle peculiar PSF shapes that are sometimes encountered in adaptive optics images (Bennett et al. 2010b). The initial DAOPHOT reduction did not detect the fainter component of the source plus lens star blend, and this resulted in the residual image shown in Figure 1(c) when the best fit PSF model was subtracted from the original image (shown in Figures 1(a) and (b)). Following Bhattacharya et al. (2018), we then added an additional source at the position of the brightest residual in Figure 1(c) and reran DAOPHOT. This resulted in the two stars indicated in Figure 1(b) and the two-star fit residual shown in Figure 1(d). This two-star fit residual is nearly featureless, indicating that the Keck image is well modeled by two stars separated by  $\sim 1$  FWHM. This analysis reveals that magnitudes of the two stars are  $K_S = 17.679 \pm 0.060$  and  $K_L = 18.925 \pm 0.062$ , where the uncertainty is dominated by the calibration uncertainty. The identification of the brighter star as the source star is determined from the predicted  $K$ -band brightness of the source star.

In order to determine which star is the source and which is the candidate lens star, we need to compare to the light curve predictions. The Dong et al. (2009b) paper gives magnitudes and colors based on an early version of the OGLE-III survey calibrations and uses old values for the intrinsic color and magnitude of red clump giant stars to estimate the extinction. We redo this analysis with updated OGLE-III light curves, the final OGLE-III magnitude and color calibrations (Szymański et al. 2011), and the Nataf et al. (2013) values for the properties of the bulge red clump giant stars at the Galactic position ( $l = -4.4198^\circ$ ,  $b = -3.7864^\circ$ ) of the target. Using standard methods (Bennett et al. 2010b), we find the centroid of the red clump for stars within  $2'$  of the source to be  $[(V - I)_{\text{RC}}, I_{\text{RC}}] = [1.85, 15.71]$ . Based on the intrinsic red clump giant stars from Nataf et al. (2013), this gives a color excess of  $E(V - I) = 0.79$  and  $I$ -band extinction of  $A_I = 1.10$ , which together imply  $V$ -band extinction of  $A_V = 1.89$ . The  $K$ -band extinction was determined to be  $A_K = 0.15$  from the online VVV extinction calculator (Gonzalez et al. 2011) using the Nishiyama et al. (2009) extinction law. From the best fit constrained light curve model, described in Section 4, we find a source color of  $V_S - I_S = 1.43$ , so the extinction corrected color is  $V_{S0} - I_{S0} = 0.64$ . Using the color-color relations of Kenyon & Hartmann (1995) and the  $I$ -band magnitude,  $I_S = 19.54$  from this same model, we predict a source magnitude of  $K_S = 17.89$ . This can only be consistent with the brighter of the two blended stars shown in Figures 1(a) and (b), although it is fainter by about  $3\text{-}\sigma$ , which suggests that the source might have a faint companion.

### 3. The Lens-Source Relative Proper Motion

The measured offset of the lens star with respect to the source is  $\Delta\text{RA} = -41.5 \pm 1.3$  mas and  $\Delta\text{DEC} = 36.1 \pm 1.3$  mas. The Keck observations were taken on 28 May 2019, which was 14.103 years after the event. The apparent motion relative motion of the lens and source is primarily due to their space motions, but there is also a contribution from parallax due to the orbital motion of the Earth. However, this contribution is  $\lesssim 0.2$  mas for a lens more distant than  $D_L \gtrsim 2$  kpc. We can ignore this contribution, because it is much smaller than the error bars on our position

measurements, so the lens-source relative proper motion is

$$\boldsymbol{\mu}_{\text{rel,H}} = (\mu_{\text{rel,H,E}}, \mu_{\text{rel,H,N}}) = (-2.945 \pm 0.091, 2.563 \pm 0.091) \text{ mas/yr} , \quad (1)$$

where the subscript H indicates that this is the proper motion in the Heliocentric reference frame, while the E and N subscripts indicate the East and North directions. We can also convert these relative proper motions to galactic coordinates:

$$\boldsymbol{\mu}_{\text{rel,H}} = (\mu_{\text{rel,H},l}, \mu_{\text{rel,H},b}) = (0.703 \pm 0.091, 3.840 \pm 0.091) \text{ mas/yr} . \quad (2)$$

The uncertainties in the separation measurements were calculated following King (1983), using the equation

$$\sigma_x = 0.65238 \times \text{FWHM} \times \sqrt{\frac{4}{3}} \times \frac{\sigma_F}{F} \quad (3)$$

where  $F$  and  $\sigma_F$  are the flux and error bar for the star with the measured position.

### 3.1. Source and Lens Proper Motion

In addition to the lens-source relative proper motion, we can also compare the astrometry of our 2019 Keck images to the astrometry of Hubble Space Telescope (HST) images taken in 2005 and 2006 (Dong et al. 2009b). We select the 2005  $V$ -band (F555W) images taken 14.013 years before the Keck images because these will provide a negligible parallax signal while providing a precise position for source star, since the lens-source separation is quite small one month after the event peak, and the source was still magnified by a factor of  $\sim 2$  and is much brighter than the lens in the  $V$ -band. The HST data was reduced with DOLPHOT (Dolphin 2000) which does not produce astrometry with precision that is quite as high as the method of Anderson & King (2000, 2004, 2006), but this will have little influence on the final proper motion results, because the uncertainties are dominated by the uncertainties in the Gaia astrometry.

There are three relatively bright stars within  $5''$  of the OGLE-2005-BLG-071 microlensing event with proper motion measurements in the Gaia DR2 data release (Gaia Collaboration et al. 2018). These stars have Gaia numbers 4041487538966873216, 4041487538966873344, and 4041487538966886016, and their  $V$ -band magnitudes are 18.399, 18.238, and 16.953. This allows us to determine the source proper motions in Galactic coordinates:

$$\boldsymbol{\mu}_S = (\mu_{S,l}, \mu_{S,b}) = (-4.99 \pm 0.19, -0.69 \pm 0.25) \text{ mas/yr} , \quad (4)$$

where  $l$  and  $b$  refer to Galactic longitude and latitude. We can then add  $\boldsymbol{\mu}_S$  and  $\boldsymbol{\mu}_{\text{rel,H}}$  from equation 2 to determine the lens proper motion,

$$\boldsymbol{\mu}_L = (\mu_{L,l}, \mu_{L,b}) = (-3.14 \pm 0.21, 3.38 \pm 0.27) \text{ mas/yr} . \quad (5)$$

The source proper motion,  $\boldsymbol{\mu}_S$ , is dominated by the reflex motion of Galactic rotation and is quite typical for the proper motion of Galactic bulge star.

Dong et al. (2009b) claimed that the OGLE-2005-BLG-071L lens star had the kinematics of a thick disk star. If true, this would be a surprise because super-Jupiter mass planets are thought to form preferentially around more massive, high metallicity star. Thick disk stars tend to have low metallicity, so it would be surprising if OGLE-2005-BLG-071Lb was a super-Jupiter mass planet orbiting a low-mass, low metallicity star (Fischer, & Valenti 2005). The Dong et al. (2009b) claim of thick disk kinematics is based upon their claim of velocity with respect to the local standard of rest of  $v_{\text{LSR}} = 103 \pm 15$  km/sec. We can compare this to our measurement of the lens star transverse velocity if we assume a lens distance  $D_L = 3.5$  kpc, which is the favored  $D_L$  according to the analysis presented below in Section 5. We find a transverse velocity of  $\mathbf{v}_L = (v_{L,l}, v_{L,b}) = (-52.5, 56.5)$  km/sec for a total transverse velocity of 77 km/sec. This is within  $2\text{-}\sigma$  of the Dong et al. (2009b)  $v_{\text{LSR}}$ , but in fact, Dong et al. (2009b) do not specify that their  $v_{\text{LSR}}$  value refers to a transverse velocity, so it is probably supposed to be a full three-dimensional velocity, with the unmeasured radial component just an estimate from averaging over a Galactic model. This would imply that their  $v_{\text{LSR}}$  value is probably consistent with our measured 77 km/sec transverse velocity. However, their conclusion that the OGLE-2005-BLG-071L has thick disk kinematics does not follow.

The Gaia DR2 data release enables a much more accurate test of the kinematic properties for stars that are a few kpc from the Sun. In particular, the Gaia Collaboration et al. (2018) study of the Milky Way disk kinematics provides valuable information on the kinematic properties of stars in the vicinity of OGLE-2005-BLG-071L, located at a distance of  $D_L \sim 3.5$  kpc toward the Galactic bulge at  $\sim 0.22$  kpc below the Galactic plane. Figure 11 of Gaia Collaboration et al. (2018) indicates that the median orbital velocity in the disk has dropped to  $v_\phi = 205$  km/sec compared to  $v_\phi = 240$  km/sec at the Solar circle. This means that the velocity of OGLE-2005-BLG-071L compared to the stars in its vicinity  $\mathbf{v}_{L,\text{VSR}} = (-17.5, 56.5)$  km/sec (where VSR stands for vicinity standard of rest). The median stellar velocity in the  $z$  direction (perpendicular to the Galactic disk) doesn't differ from the median velocity of 0 at the Solar circle, but the velocity dispersions in both directions grow to  $\sigma_{v_\phi} = 45$  km/sec and  $\sigma_{v_z} = 38$  km/sec. Thus, the  $l$  and  $b$  components of  $\mathbf{v}_L$  are  $0.4\sigma$  and  $1.5\sigma$  from the center of the velocity distribution. So, we conclude that OGLE-2005-BLG-071L has normal stellar kinematics for a star at its location, and it should not be considered to be a thick disk star.

### 3.2. Geocentric Relative Proper Motion

Our light curve modeling is done in a geocentric reference frame that differs from the heliocentric frame by the instantaneous velocity of the Earth at the time of peak magnification. This avoids large correlated uncertainties for the light curve parameters that would be quite common for models done in the heliocentric frame. However, this also means that the lens-source relative proper motion that we measure with follow-up observations is not in the same reference frame as the light curve parameters. This is an important issue because, as we show below, the measured



relative proper motion can be combined with the microlensing parallax light curve parameter to determine the mass of the lens system. The relation between the relative proper motions in the heliocentric and geocentric coordinate systems are given by (Dong et al. 2009b):

$$\boldsymbol{\mu}_{\text{rel,H}} = \boldsymbol{\mu}_{\text{rel,G}} + \frac{\mathbf{v}_{\oplus}\pi_{\text{rel}}}{\text{AU}} , \quad (6)$$

where  $\mathbf{v}_{\oplus}$  is the projected velocity of the Earth relative to the Sun (perpendicular to the line-of-sight) at the time of peak magnification. The projected velocity for OGLE-2005-BLG-071 is  $\mathbf{v}_{\oplus\text{E,N}} = (15.508, 4.685) \text{ km/sec} = (3.271, 0.988) \text{ AU/yr}$  at the peak of the microlensing light curve, HJD' = 3480.70. The relative parallax is defined as  $\pi_{\text{rel}} \equiv 1/D_L - 1/D_S$ , where  $D_L$  and  $D_S$  are lens and source distances, so equation 6 can be written as:

$$\boldsymbol{\mu}_{\text{rel,G}} = \boldsymbol{\mu}_{\text{rel,H}} - (3.271, 0.988) \times (1/D_L - 1/D_S) ,$$

which is a more convenient form since  $\boldsymbol{\mu}_{\text{rel,H}}$  has been measured directly from the Keck images. Now at each possible lens distance, we can use the  $\mu_{\text{rel,G}}$  value from equation 6 to determine the angular Einstein radius,  $\theta_E = \mu_{\text{rel,G}} t_E$ . As we explain below, the  $\boldsymbol{\mu}_{\text{rel,G}}$  can also be used to convert a one-dimensional microlensing parallax measurement into a full measurement of the microlensing parallax vector. The lens flux and  $\boldsymbol{\mu}_{\text{rel,H}}$  measurements from the Keck observations and the 1-D parallax measurement constrain the angular Einstein radius, the microlensing parallax vector and, therefore, the mass and distance of the lens system.

Table 1 shows the parameters of our four degenerate light curve models and the Markov Chain average of all four models without constraints from the Keck or HST observations. The parameters that apply to single lens models are the Einstein radius crossing time,  $t_E$ , the time of closest

Table 1. Best Fit Unconstrained Model Parameters

parameter	$u_0 < 0$		$u_0 > 0$		MCMC averages
	$s < 1$	$s > 1$	$s < 1$	$s > 1$	
$t_E$ (days)	77.100	70.942	72.324	69.825	$71.8 \pm 3.2$
$t_0$ (HJD')	3480.7048	3480.7048	3480.6971	3480.6971	$3480.702 \pm 0.004$
$u_0$	-0.021476	-0.027294	0.027680	0.023016	$0.006 \pm 0.025$
$s$	0.75384	1.29784	0.75805	1.29140	$1.15 \pm 0.24$
$\alpha$ (rad)	-1.65212	-1.64712	1.65041	1.64547	$-0.40 \pm 1.60$
$q \times 10^3$	6.5824	7.1689	6.8499	7.1594	$6.98 \pm 0.29$
$t_*$ (days)	0.01026	0.01652	0.02106	0.03092	$0.018 \pm 0.012$
$\pi_{\text{E,N}}$	-0.9150	-0.6331	0.08204	-0.1065	$-0.42 \pm 0.41$
$\pi_{\text{E,E}}$	-0.3692	-0.3058	-0.21894	-0.2311	$-0.279 \pm 0.066$
fit $\chi^2$	1241.91	1226.24	1250.50	1231.14	

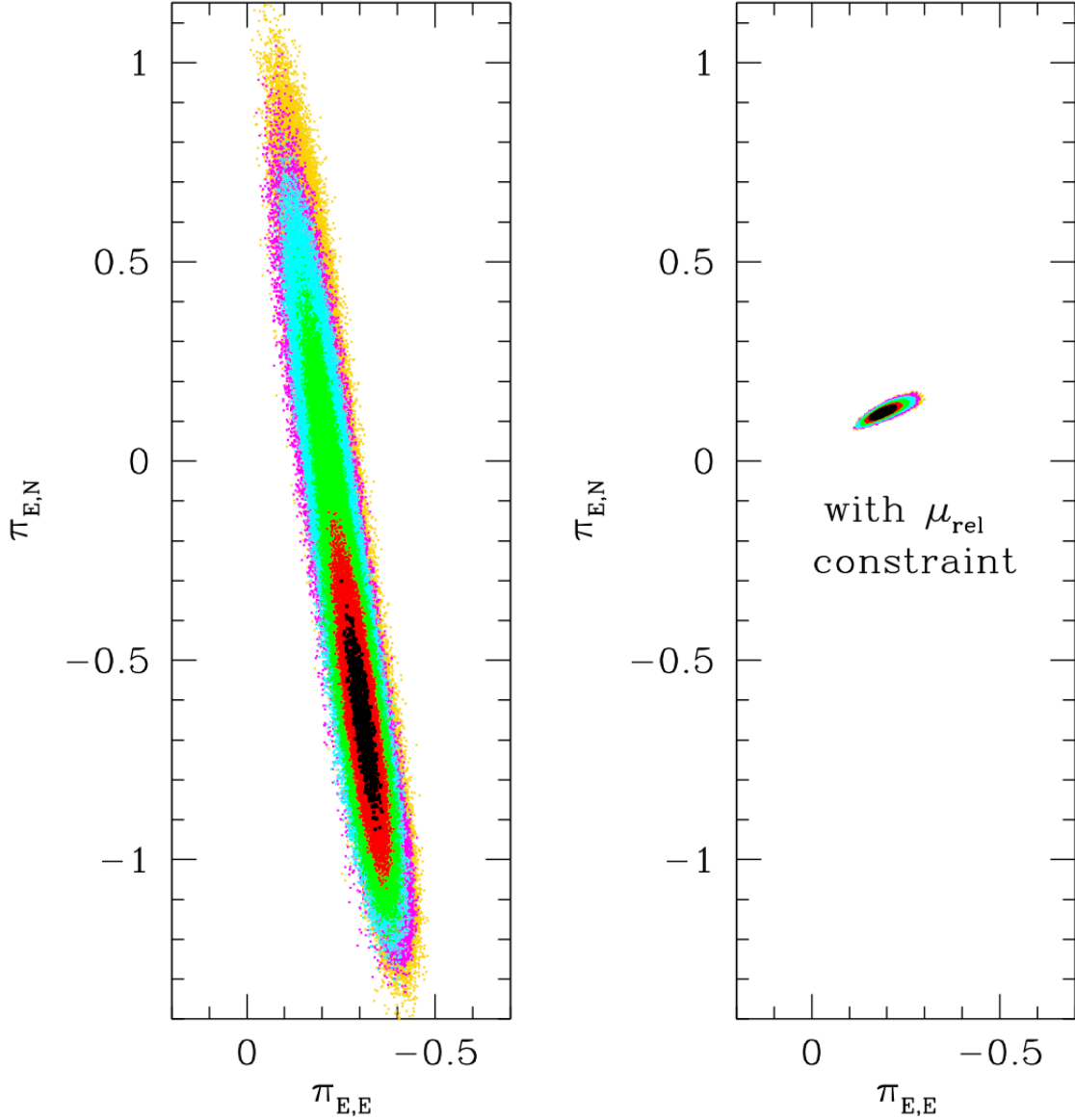


Fig. 2.— *Left panel:* The  $\pi_E$  distribution from light curve modeling without any constraint from follow-up observations. *Right panel:* The  $\pi_E$  distribution resulting from the addition of the high resolution follow-up imaging constraints. The following color scheme is used to denote the  $\chi^2$  differences from the best fit light curve model: black represents  $\Delta\chi^2 < 1$ , red represents  $\Delta\chi^2 < 4$ , green represents  $\Delta\chi^2 < 16$ , cyan represents  $\Delta\chi^2 < 25$ , and magenta represents  $\Delta\chi^2 \geq 25$ . The right panel clearly shows that the relative proper motion measurements from Keck constrain  $\pi_{E,N}$ , which is the North component of  $\pi_E$ , that was largely unconstrained by the light curve. Without the  $\mu_{\text{rel,H}}$  measurement, in the left panel, the light curve slightly favors solutions with  $\pi_{E,N} < 0$ , but the constraint forces  $\pi_{E,N} > 0$ . Note that this figure combines all four of the degenerate models.

alignment between the source and the lens system center-of-mass,  $t_0$ , and the distance of closest approach between the source and the lens system center-of-mass,  $u_0$ , which is given in units of the Einstein radius. The addition of a second lens mass requires three additional parameters, the mass ratio of the two lens masses,  $q$ , their separation,  $s$ , in units of the Einstein radius, and the angle,  $\alpha$ , between the source trajectory and the transverse line that passes through the two lens masses. In addition, a large fraction of binary lens systems exhibit finite source effects that can be modeled with the addition of the source radius crossing time parameter,  $t_*$ . In addition to these parameters, we also have parameters for the source flux and blended flux for each data set that are fit linearly to each light curve model, following Rhie et al. (1999). For high magnification events, like OGLE-2005-BLG-071, the transformation  $s \rightarrow 1/s$  often has only a slight change on the shape of the light curve. This is known as the close-wide degeneracy, and it applies to OGLE-2005-BLG-071 (Udalski et al. 2005; Dong et al. 2009b).

Many longer duration binary lens events, like OGLE-2005-BLG-071, exhibit light curve effects due to the orbital motion of the Earth during the event. This is known as the microlensing parallax effect, and Dong et al. (2009b) have shown that OGLE-2005-BLG-071 has a significant signal, which is described by a two-dimensional vector,  $\boldsymbol{\pi}_E$ , that is parallel to the direction of lens-source relative motion. The inclusion of the microlensing parallax parameters introduces an additional degeneracy. Without microlensing parallax, the transformation  $u_0 \rightarrow -u_0$ ,  $\alpha \rightarrow -\alpha$  produces exactly the same light curve, and it can just be thought of as a change of parameters. When microlensing parallax is added, however, this transformation amounts to a reflection of the lens system orientation with respect to the orbit of the Earth, so it is no longer a trivial, exact degeneracy (unless the lens system lies in the ecliptic plane). This second degeneracy is often referred to as the  $u_0 \leftrightarrow -u_0$  degeneracy. We do not include lens orbital motion for these unconstrained models, which we consider only to offer a comparison to the models with constraints from high angular resolution follow-up observations.

#### 4. Relative Proper Motion Constraints on $\boldsymbol{\pi}_E$ and Light Curve Models

As Figure 2 indicates, the microlensing light curve provides a fairly tight constraint on one component of the microlensing parallax vector,  $\boldsymbol{\pi}_E$ . This is the component in the direction of the Earth’s acceleration, which is nearly parallel to the East-West direction. But as it is often the case (Muraki et al. 2011), only the  $\pi_{E,E}$  component of the microlensing parallax vector is measured precisely. As shown in the left panel of Figure 2, the  $2\text{-}\sigma$  range for  $\pi_{E,N}$  is  $-0.39 < \pi_{E,N} < 0.43$ . However, the microlensing parallax vector,  $\boldsymbol{\pi}_E$  is parallel to the  $\boldsymbol{\mu}_{\text{rel,G}}$  vector, and the two quantities are related by

$$\boldsymbol{\pi}_E = \frac{\pi_{\text{rel}}}{t_E} \frac{\boldsymbol{\mu}_{\text{rel,G}}}{|\boldsymbol{\mu}_{\text{rel,G}}|^2}, \quad (7)$$

so with measurements of  $\pi_{E,E}$  and  $\boldsymbol{\mu}_{\text{rel,H}}$ , we can use equations 6 and 7 to solve for  $\pi_{E,N}$  (Bennett et al. 2007). While this leads to a quadratic equation, Bhattacharya et al. (2018) have shown that

there is only a single physically plausible solution of this equation for virtually all microlensing events observed towards the Galactic bulge.

The volume of the light curve model parameter space that is allowed by the Keck observation constraints on  $\mu_{\text{rel,H}}$  and  $K_L$  is very much smaller than the volume allowed without those constraints as Figure 2 indicates. As a result, we would have poor sampling of the posterior distributions if we were to apply these constraints to Markov Chains that were run without any constraints based on the Keck observations. So, following Bhattacharya et al. (2018) we implement constraints on  $\mu_{\text{rel,H}}$  and  $K_L$  during the light curve modeling. The relative proper motion,  $\mu_{\text{rel,H}}$ , is constrained by the measurement given in equation 1, and we constrain the lens star  $K$ -band brightness to be  $K_L = 18.925 \pm 0.062$ , as discussed in Section 2. Following Bhattacharya et al. (2018), these constraints are implemented a  $\chi^2$  contribution from each of the constraints and adding it to the light curve fit  $\chi^2$  inside the modeling code (Bennett 2010). We use the empirical mass-luminosity relation described by Bennett et al. (2018b), which is a combination of several different mass-luminosity relations for different mass ranges. For  $M_L \geq 0.66 M_\odot$ ,  $0.54 M_\odot \geq M_L \geq 0.12 M_\odot$ , and  $0.10 M_\odot \geq M_L \geq 0.07 M_\odot$ , we use the relations of Henry & McCarthy (1993), Delfosse et al. (2000), and Henry et al. (1999), respectively. In between these mass ranges, we linearly interpolate between the two relations used on the boundaries. That is, we interpolate between the Henry & McCarthy (1993) and the Delfosse et al. (2000) relations for  $0.66 M_\odot > M_L > 0.54 M_\odot$ , and we interpolate between the Delfosse et al. (2000) and Henry et al. (1999) relations for  $0.12 M_\odot > M_L > 0.10 M_\odot$ .

For the mass-luminosity relations, we must also consider the foreground extinction. At a Galactic latitude of  $b = -3.7865^\circ$ , and a lens distance of  $\sim 2$  kpc, the lens system is likely to be behind some, but not all, of the dust that is in the foreground of the source. We assume a dust scale height of  $h_{\text{dust}} = 0.10 \pm 0.02$  kpc, so that the extinction in the foreground of the lens is given by

$$A_{i,L} = \frac{1 - e^{-|D_L(\sin b)/h_{\text{dust}}|}}{1 - e^{-|D_S(\sin b)/h_{\text{dust}}|}} A_{i,S} , \quad (8)$$

where the index  $i$  refers to the passband:  $I$ ,  $V$ , or  $K$ . (Constraints on the lens plus source brightness from the HST  $I$  and  $V$ -band observations will be applied when combining the MCMC calculations with Bayesian priors.) In the Markov Chain calculations themselves, we fix  $D_S = 8.8$  kpc for our source star at a Galactic longitude of  $l = -4.4198^\circ$ , and we fix the dust scale height at  $h_{\text{dust}} = 0.10$  kpc. But, we remove these restrictions by reweighting the links in the Markov Chain when we sum them for our final results.

In addition to these constraints, we also include two additional parameters to describe the orbital motion of the planet. Unlike the case of the two planet event OGLE-2006-BLG-109 (Gaudi et al. 2008; Bennett et al. 2010b), the light curve does not provide significant constraints on the planetary orbital motion. However, like the case of MOA-2009-BLG-266 (Muraki et al. 2011), the inclusion of orbital motion does affect the relative weighting of the degenerate models. In particular, the inclusion of orbital motion substantially decreases the  $\chi^2$  difference between the wide and close models, which are only disfavored by  $\Delta\chi^2 \approx 4.3$  for the constrained models. This can be seen by

a comparison of the  $\chi^2$  difference between the wide and close models for the constrained model, shown in Table 2 and the unconstrained models without orbital motion, shown in Table 1. As was the case with MOA-2009-BLG-266, the  $\chi^2$  difference between the  $u_0 > 0$  and  $u_0 < 0$  solutions is also decreased.

While these constraints have little effect on the best fit model  $\chi^2$ , they have a dramatic effect on the allowed range of microlensing parallax parameters, as Figure 2 indicates. The  $2\text{-}\sigma$  range for  $\pi_{E,N}$  is reduced from  $-1.07 < \pi_{E,N} < 0.49$  to  $0.104 < \pi_{E,N} < 0.144$ , which is a reduction of a factor of 39 in uncertainty. This yields a microlensing parallax amplitude of  $\pi_E = 0.229 \pm 0.023$ , which will be used in Section 5 to determine the lens mass.

## 5. Lens Properties

The situation for OGLE-2005-BLG-071 is similar to the case of OGLE-2012-BLG-0950 (Bhattacharya et al. 2018) in that the source radius crossing time,  $t_*$ , has not been reliably measured. Fortunately, as discussed above in Section 3.2, it is straight forward to constrain the angular Einstein radius,  $\theta_E$ , with our measurement of  $\mu_{\text{rel,H}}$  given in equations 1 and 2. The conversion between the heliocentric and geocentric frames only provides a minor complication. The geocentric relative

Table 2. Best Fit Model Parameters with  $\mu_{\text{rel}}$  and Magnitude Constraints

parameter	$u_0 < 0$		$u_0 > 0$		MCMC averages
	$s < 1$	$s > 1$	$s < 1$	$s > 1$	
$t_E$ (days)	68.357	68.221	68.420	67.912	$68.1 \pm 1.2$
$t_0$ (HJD')	3480.6751	3480.6919	3480.6755	3480.6922	$3480.692 \pm 0.007$
$u_0$	-0.024468	-0.028289	0.024401	0.028439	$0.001 \pm 0.028$
$s_0$	0.76151	1.28821	0.76067	1.28956	$1.233 \pm 0.163$
$\alpha$ (rad)	-1.64182	-1.64233	1.64218	1.64267	$0.06 \pm 1.64$
$q \times 10^3$	7.0943	7.2753	7.1262	7.3421	$7.32 \pm 0.16$
$t_*$ (days)	0.05103	0.05113	0.05087	0.05143	$0.0513 \pm 0.0014$
$\pi_{E,N}$	0.1223	0.1234	0.1218	0.1204	$0.123 \pm 0.010$
$\pi_{E,E}$	-0.1899	-0.1913	-0.1685	-0.1909	$-0.192 \pm 0.021$
$\dot{s}_x$ (days $^{-1}$ )	0.00139	-0.00126	0.00139	-0.00128	$-0.00081 \pm 0.00084$
$\dot{s}_y$ (days $^{-1}$ )	-0.00187	-0.00128	0.00173	0.00102	$-0.00002 \pm 0.00081$
$I_s$	19.550	19.543	19.554	19.539	$19.542 \pm 0.026$
$V_s$	20.981	20.975	20.971	20.986	$20.974 \pm 0.026$
fit $\chi^2$	1234.29	1230.13	1234.27	1229.98	

proper motion,  $\boldsymbol{\mu}_{\text{rel,G}}$ , is determined directly from  $\boldsymbol{\mu}_{\text{rel,H}}$  with only a minor correction due to the lens distance. We can then determine the angular Einstein radius from  $\theta_E = t_E \mu_{\text{rel,G}}$ . As discussed in Section 4, the measurement of  $\boldsymbol{\mu}_{\text{rel,H}}$  also allows us to determine the full microlensing parallax vector,  $\boldsymbol{\pi}_E$ , when the light curve has only determined one component of the vector using equations 6 and 7.

Measurements of either angular Einstein radius,  $\theta_E$ , or the microlensing parallax amplitude,  $\pi_E$ , provide mass-distance relations (Bennett 2008; Gaudi 2012),

$$M_L = \frac{c^2}{4G} \theta_E^2 \frac{D_S D_L}{D_S - D_L} = \frac{c^2}{4G} \frac{\text{AU}}{\pi_E^2} \frac{D_S - D_L}{D_S D_L}, \quad (9)$$

which can be combined to yield the lens mass in an expression with no dependence on the lens or source distance,

$$M_L = \frac{c^2 \theta_E \text{AU}}{4G \pi_E} = \frac{\theta_E}{(8.1439 \text{ mas}) \pi_E} M_\odot. \quad (10)$$

Our measurement of the host star  $K$ -band magnitude,  $K_L$ , also implies a mass-distance relation when combined with our empirical mass-luminosity relation, and the HST observation in 2005 and 2006 (Dong et al. 2009b) provide upper limits on the host star brightness in the  $I$  and  $V$  bands.

To solve for the planetary system parameters with all these constraints, we sum over our MCMC results using the Galactic model employed by Bennett et al. (2014) as a prior, weighted by the microlensing rate and the measured  $\boldsymbol{\mu}_{\text{rel,H}}$  value. The lens magnitude measurements were applied as constraints in the light curve modeling, so we do not apply them again in the sum over the MCMC results. We do constrain the source distances to follow the microlensing rate weighted distribution according to our Galactic model, and we evaluate the extinction in the foreground of the lens using equation 8 with the assumed error bar for  $h_{\text{dust}}$ . The Galactic model is used to properly weight the source distances.

Figure 3 and Table 3 provide the results of our analysis. We find that the host star has a mass

Table 3. Measurement of Planetary System Parameters from the Lens Flux Constraints

parameter	units	value & RMS	2- $\sigma$ range
Angular Einstein Radius, $\theta_E$	mas	$0.793 \pm 0.042$	0.710–0.876
Geocentric lens-source relative proper motion, $\mu_{\text{rel,G}}$	mas/yr	$4.25 \pm 0.21$	3.84–4.66
Host star mass, $M_{\text{host}}$	$M_\odot$	$0.426 \pm 0.037$	0.357–0.506
Planet mass, $m_p$	$M_{\text{Jup}}$	$3.27 \pm 0.32$	2.70–3.96
Host star - Planet 2D separation, $a_\perp$	AU	$3.38 \pm 0.52$	1.95–4.08
Host star - Planet 3D separation, $a_{3d}$	AU	$4.0^{+2.3}_{-0.6}$	2.1–14.3
Lens distance, $D_L$	kpc	$3.46 \pm 0.33$	2.85–4.18

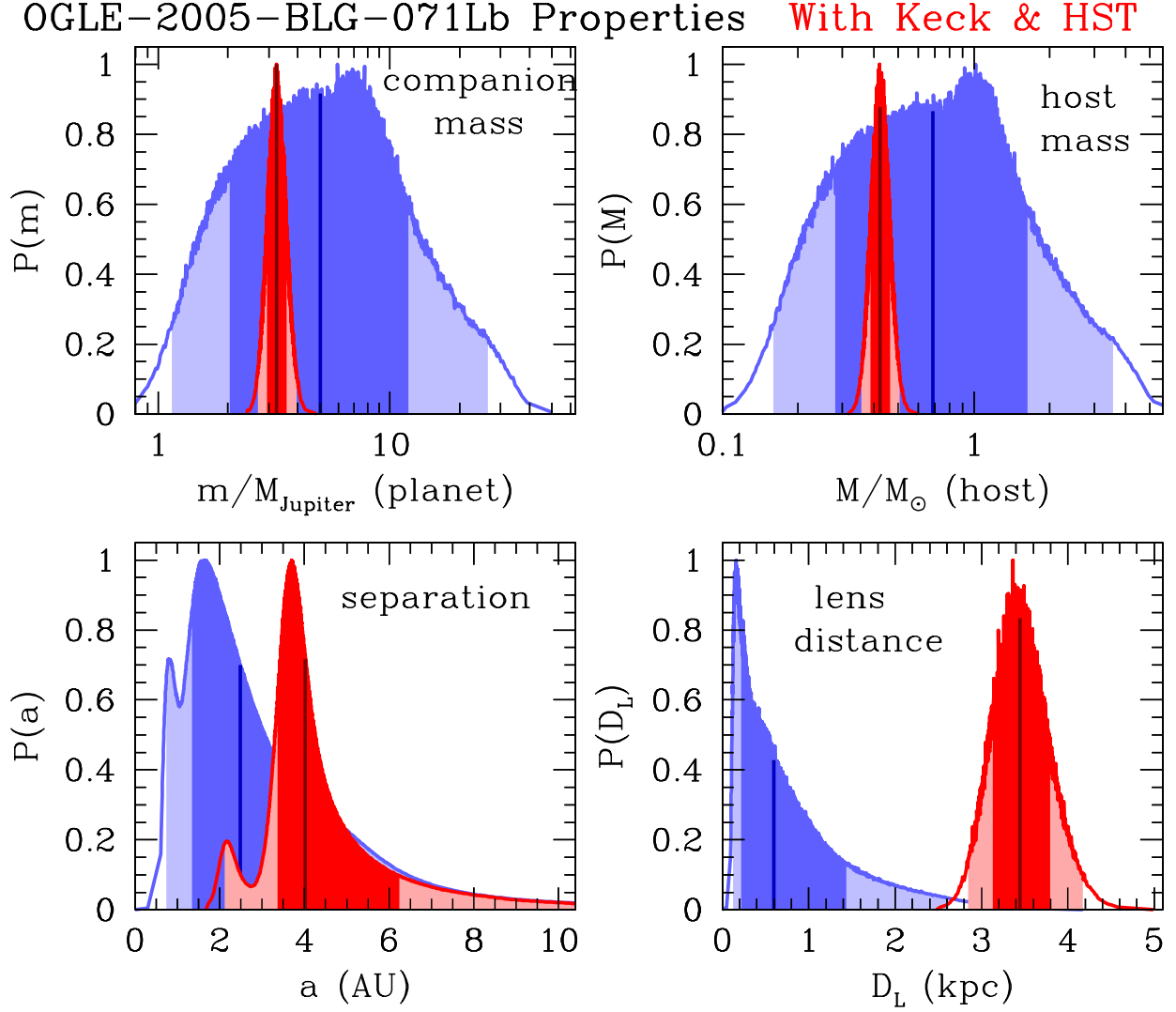


Fig. 3.— The Bayesian posterior probability distributions for the planetary companion mass, host mass, their separation and the distance to the lens system are shown with only light curve constraints in blue and with the additional constraints from our Keck and HST follow-up observations in red. The central 68.3% of the distributions are shaded in darker colors (dark red and dark blue) and the remaining central 95.4% of the distributions are shaded in lighter colors. The vertical black line marks the median of the probability distribution of the respective parameters.

of  $M_{\text{host}} = 0.43 \pm 0.04 M_{\odot}$  and it is orbited by a super-Jupiter mass planet with  $m_p = 3.3 \pm 0.3 M_{\text{Jup}}$  at a projected separation of  $a_{\perp} = 3.4 \pm 0.5$  AU. This translates to a three-dimensional separation of  $a_{3d} = 4.0^{+2.3}_{-0.6}$  AU under the assumption of a random orientation of the planetary orbit, and the lens system is located at a distance of  $D_L = 3.5 \pm 0.3$  kpc. These distributions are indicated by the red histograms in Figure 3. These results are a dramatic improvement in precision over blue histograms that indicate the parameters predicted by our Bayesian analysis without any constraints from Keck or HST observations. However, the lens distance distribution predicted by the unconstrained analysis is peculiar with its sharp peak at very small distances. This is due to the light curve preference for very small source radius crossing time,  $t_*$ , values. We suspect that this is due to systematic errors in the Auckland Observatory photometry. As discussed by Dong et al. (2009b), the flat field images from this telescope had serious scattered light problems that were exacerbated by a  $180^\circ$  flip of the telescope orientation in the middle of each night. Also, the observations were unfiltered, which led to photometry errors as large as 7% due to differential atmospheric chromatic extinction. It is possible that some of these systematic errors remain after Dong et al. (2009b) attempted to correct them. For example, their correction for differential chromatic extinction implicitly assumed that the atmospheric chromatic extinction effects remained constant over all four days when the event was at its peak, but the water vapor and aerosol composition of the atmosphere might have changed during that period. This problem was mitigated in the Dong et al. (2009b) analysis by the constraints they placed on the lens brightness and a crude constraint they placed on the lens-source relative proper motion from the color-dependent centroid shift effect (Bennett et al. 2006).

### 5.1. Comparison to Previous Analysis

Our conclusions are largely in line with those of Dong et al. (2009b), except that we do not have to make the assumption that the unlensed light coincident with the source in the 2005 and 2006 HST images is not due to a source companion. While our Keck data are consistent with the existence of a faint source companion, our measurement of the  $K$ -band lens brightness indicates excess  $I$  and  $V$ -band flux seen in the HST images is primarily due to the lens star.

The one Dong et al. (2009b) claim that clearly seems to be incorrect is the claim that the OGLE-2005-BLG-071L planetary host star has thick disk kinematics. Dong et al. (2009b) do not provide many details about how they reach this conclusion, but a primary difference appears to be the fact that they compare their estimated lens velocity to the local standard of rest rather than the kinematics of the Galaxy at location of the lens, which was understood only recently (Gaia Collaboration et al. 2018).

It is also of interest to consider the accuracy of their measurement of the color dependent centroid shift measurement (Bennett et al. 2006), since this is of interest for WFIRST (Bhattacharya et al. 2018). They measure offsets between the target (source plus lens blend) centroid in the  $I$  and  $V$ -band magnitudes of  $\Delta r_{I-V,E} = -0.52 \pm 0.20$  mas and  $\Delta r_{I-V,N} = 0.22 \pm 0.20$  mas in the East



and North directions, respectively. However, this includes both proper motion and parallax, so to compare to our measurements, we must convert this measurement to the heliocentric reference frame. With our estimate of the lens system distance,  $D_L$ , the centroid shift becomes  $\Delta r_{I-V,E,H} = -0.45 \pm 0.20$  mas and  $\Delta r_{I-V,N,H} = 0.22 \pm 0.20$  mas. We can compare this to the value determined from our precise Keck  $\mu_{\text{rel},H}$  measurements. At the time of the 2006 HST observations, we find  $\Delta r_{I-V,E,H} = -0.115 \pm 0.003$  mas and  $\Delta r_{I-V,N,H} = 0.100 \pm 0.003$  mas, so the HST estimates are off by  $1.7\sigma$  to the East and  $0.5\sigma$  to the North. This suggests that the estimated error bars are not likely to be underestimated by as much as a factor of 2.

## 6. Discussion and Conclusions

Our Keck AO follow-up observations have identified the OGLE-2005-BLG-071L planetary host star through measurements of the lens  $K$ -band magnitude, and the lens-source relative proper motion,  $\mu_{\text{rel},H}$ . These measurements allow the determination of the lens mass and distance through multiple, redundant constraints. The  $\mu_{\text{rel},H}$  measurement can be combined with the partial microlensing parallax measurement from the microlensing light curve to yield the lens system masses, and the  $\mu_{\text{rel},H}$  measurement can also be combined with the lens  $K$ -band magnitude to yield the lens mass and distance, as well. These determinations are consistent with each other, and we combine them to give host and planet masses of  $M_{\text{host}} = 0.426 \pm 0.037 M_{\odot}$ , and  $m_p = 3.27 \pm 0.32 M_{\text{Jup}}$ , with a projected separation of  $a_{\perp} = 3.38 \pm 0.52$  AU at a distance of  $D_L = 3.46 \pm 0.33$  kpc. The excess flux seen in 2005 and 2006 HST observations is also consistent with these conclusions.

This confirms that tentative conclusion of Dong et al. (2009b) that this event is a somewhat unexpected sample of a super-Jupiter mass planet orbiting an M-dwarf. Such planetary systems are thought to be rare (Laughlin et al. 2004). Since the wide model is slightly favored, the preferred orbital period is 12 years or more, and this means that many exoplanet Doppler radial velocity surveys do not monitor their stars long enough to detect such planets. However, those surveys that do monitor the radial velocity of low-mass stars for long periods of time claim a low frequency of such planets (Johnson et al. 2010), although they have not yet done a complete statistical analysis. The microlensing statistical analysis of Suzuki et al. (2016, 2018) seems quite consistent with the preliminary radial velocity results since it includes two planets with mass ratios of  $q \sim 7 \times 10^{-3}$ , when we would expect  $\sim 700$  if there was an average of one such planet orbiting every star. So, we might expect an occurrence rate for such planets of 1/300 or 1/400. The other similar planet in the Suzuki et al. (2016) sample is MOA-2008-BLG-379 (Suzuki et al. 2014,e).

It is expected that the occurrence rate for super-Jupiter planets should be higher for planets that orbit high metallicity host stars (Fischer, & Valenti 2005). Because the host star, OGLE-2005-BLG-071L, can now be resolved from the source star in  $K$ -band AO images, it should now be possible to determine the host star metallicity with moderate resolution  $K$ -band spectra (Rojas-Ayala et al. 2010) using instruments such as Keck/OSIRIS and VLT/MUSE. Both of these instruments employ AO feeds and OH suppression that are probably required for spectra of sufficient S/N to

measure metallicity.

Finally, we should mention that this event is part of our Keck Key Strategic Mission Support (KSMS) program that aims to determine masses and distances for the vast majority of stars in the Suzuki et al. (2016) sample, as well as the MOA 9-year microlensing event sample that is now under analysis. One important of this program is that it can test an assumption that is currently used to estimate the host mass for most of the planets found by microlensing (Beaulieu et al. 2006; Dong et al. 2009a). For this event, a sub-Saturn mass planet (Bhattacharya et al. 2018), and a Uranus-mass planet (Bennett et al. 2015; Batista et al. 2015), we find that the measured host star mass is close to the Bayesian prediction, which relies upon the assumption that stars of any mass are equally likely to host the planet with the given mass ratio. This differs from the case of two other targets from our KSMS program: MOA-2007-BLG-400 (Bhattacharya et al., in preparation) and MOA-2013-BLG-220 (Vandorou et al., in preparation). The mass measurement for these two events find masses that are at the 94th and 93rd percentile Bayesian analysis prediction based on the equal planet hosting probability assumption. These events also have very similar mass ratio of  $q = 2.2 \times 10^{-3}$  and  $q = 3.3 \times 10^{-3}$ . This suggests that high mass stars may be much more likely to host planets beyond the snow line with mass ratios in the  $0.002 < q < 0.004$  range, but our OGLE-2005-BLG-071 result suggests that this trend may not hold at higher mass ratios. Clearly, more mass microlens exoplanet host star mass measurements are needed to confirm such speculation.

The Keck Telescope observations and analysis were supported by a NASA Keck PI Data Award, administered by the NASA Exoplanet Science Institute. Data presented herein were obtained at the W. M. Keck Observatory from telescope time allocated to the National Aeronautics and Space Administration through the agency's scientific partnership with the California Institute of Technology and the University of California. The Observatory was made possible by the generous financial support of the W. M. Keck Foundation. DPB and AB were also supported by NASA through grant NASA-80NSSC18K0274. This work was supported by the University of Tasmania through the UTAS Foundation and the endowed Warren Chair in Astronomy and the ANR COLD-WORLDS (ANR-18-CE31-0002). A.U. was supported by the OGLE project funded by National Science Centre, Poland with the grant MAESTRO 2014/14/A/ST9/00121.

## REFERENCES

- Anderson, J. & King, I. R. 2000, *PASP*, 112, 1360
- Anderson, J. & King, I. R. 2004, Hubble Space Telescope Advanced Camera for Surveys Instrument Science Report 04-15
- Anderson, J. & King, I. R., 2006, Hubble Space Telescope Advanced Camera for Surveys Instrument Science Report 2006-1

- Anglada-Escudé, G., Boss, A. P., Weinberger, A. J., et al. 2012, *The Astrophysical Journal*, 746, 37
- Batista, V., Gould, A., Dieters, S., et al. 2011, *A&A*, 529, A102
- Batista, V., Beaulieu, J.-P., Gould, A., et al. 2014, *ApJ*, 780, 54
- Batista, V., Beaulieu, J.-P., Bennett, D.P., et al. 2015, *ApJ*, 808, 170
- Beaulieu, J.-P., Batista, V., Bennett, D. P., et al. 2018, *AJ*, 155, 78
- Beaulieu, J.-P., Bennett, D. P., Fouqué, P., et al. 2006, *Nature*, 439, 437
- Beaulieu, J.-P., Bennett, D. P., Batista, V., et al. 2016, *ApJ*, 824, 83
- Bennett, D.P, 2008, in *Exoplanets*, Edited by John Mason. Berlin: Springer. ISBN: 978-3-540-74007-0, (arXiv:0902.1761)
- Bennett, D.P. 2010, *ApJ*, 716, 1408
- Bennett, D. P., Anderson, J., Bond, I. A., Udalski, A., & Gould, A. 2006, *ApJ*, 647, L171
- Bennett, D.P., Anderson, J., & Gaudi, B.S. 2007, *ApJ*, 660, 781
- Bennett, D. P., Batista, V., Bond, I. A., et al. 2014, *ApJ*, 785, 155
- Bennett, D. P., Bhattacharya, A., Anderson, J., et al. 2015, *ApJ*, 808, 169
- Bennett, D. P., Bond, I. A., Abe, F., et al. 2017, *AJ*, 154, 68
- Bennett, D. P., Rhie, S. H., Nikolaev, S., et al. 2010b, *ApJ*, 713, 837
- Bennett, D. P., Udalski, A., Bond, I. A., et al. 2018b, *AJ*, 156, 113
- Bertin, E., & Arnouts, S., 1996, *A&AS*, 117, 393
- Bertin, E., Mellier, Y. , Radovich, M., et al., 2002, *The TERAPIX Pipeline*, ASP Conference Series, Vol. 281, 228
- Bhattacharya, A., Beaulieu, J.-P., Bennett, D. P., et al. 2018, *AJ*, 156, 289 2014, *AJ*, 147, 47
- Carpenter, J.M. 2001, *AJ*121, 2851
- Delfosse, X., Forveille, T., Ségransan, D., et al. 2000, *A&A*, 364, 217
- Dolphin, A. E. 2000, *PASP*, 112, 1383
- Dong, S., Bond, I. A., Gould, A., et al. 2009a, *ApJ*, 698, 1826
- Dong, S., Gould, A., Udalski, A., et al. 2009b, *ApJ*, 695, 970

- Fischer, D. A., & Valenti, J. 2005, *ApJ*, 622, 1102
- Gaia Collaboration, Brown, A. G. A., Vallenari, A., et al. 2018, *A&A*, 616, A1
- Gaia Collaboration, Katz, D., Antoja, T., et al. 2018, *A&A*, 616, A11
- Gaudi, B. S. 2012, *ARA&A*, 50, 411
- Gaudi, B. S., Bennett, D. P., Udalski, A., et al. 2008, *Science*, 319, 927
- Gonzalez, O. A., Rejkuba, M., Zoccali, M., Valenti, E., & Minniti, D. 2011, *A&A*, 534, A3
- Gubler, J., & Tytler, D., 1998, *PASP*, 110, 738
- Han, C., Bennett, D. P., Udalski, A., et al. 2019, *The Astronomical Journal*, 158, 114
- Henry, T. J., Franz, O. G., Wasserman, L. H., et al. 1999, *ApJ*, 512, 864
- Henry, T. J., & McCarthy, D. W., Jr. 1993, *AJ*, 106, 773
- Hirao, Y., Udalski, A., Sumi, T., et al. 2017, *AJ*, 154, 1
- Johnson, J. A., Butler, R. P., Marcy, G. W., et al. 2007, *ApJ*, 670, 833
- Johnson, J. A., Aller, K. M., Howard, A. W., & Crepp, J. R. 2010, *PASP*, 122, 905
- Jung, Y. K., Udalski, A., Sumi, T., et al. 2015, *ApJ*, 798, 123
- Kennedy, G. M., & Kenyon, S. J. 2008, *ApJ*, 673, 502
- Kenyon, S. J., & Hartmann, L. 1995, *ApJS*, 101, 117
- King, I. R., 1983, *PASP*, 95, 163
- Koshimoto, N., Shvartzvald, Y., Bennett, D. P., et al. 2017b, *AJ*, 154, 3
- Koshimoto, N., Udalski, A., Sumi, T., et al. 2014, *ApJ*, 788, 128
- Laughlin, G., Bodenheimer, P. & Adams, F.C. 2004, *ApJ*, 612, L73
- Minniti, D., Lucas, P. W., Emerson, J. P., et al. 2010, *New A*, 15, 433
- Muraki, Y., Han, C., Bennett, D. P., et al. 2011, *ApJ*, 741, 22
- Nataf, D. M., Gould, A., Fouqué, P., et al. 2013, *ApJ*, 769, 88
- Nishiyama, S., Tamura, M., Hatano, H., et al. 2009, *ApJ*, 696, 1407
- Poleski, R., Udalski, A., Bond, I. A., et al. 2017, *A&A*, 604, A103
- Poleski, R., Udalski, A., Dong, S., et al. 2014, *The Astrophysical Journal*, 782, 47

- Rhie, S. H., Becker, A. C., Bennett, D. P., et al. 1999, *ApJ*, 522, 1037
- Rojas-Ayala, B., Covey, K. R., Muirhead, P. S., and Lloyd, J. P. 2010, *ApJ*, 720, L113
- Service, M., Lu, J. R., Campbell, R., et al. 2016, *PASP*, 128, 095004
- Shin, I.-G., Ryu, Y.-H., Udalski, A., et al. 2016, *Journal of Korean Astronomical Society*, 49, 73
- Shin, I.-G., Ryu, Y.-H., Yee, J. C., et al. 2019, *The Astronomical Journal*, 157, 146
- Shvartzvald, Y., Maoz, D., Kaspi, S., et al. 2014, *MNRAS*, 439, 604
- Street, R. A., Choi, J.-Y., Tsapras, Y., et al. 2013, *ApJ*, 763, 67
- Stetson, P. B., 1987, *PASP*, 99, 191S
- Suzuki, D., Bennett, D. P., Ida, S., et al. 2016, *ApJ*, 819, L34
- Suzuki, D., Bennett, D. P., Sumi, T., et al. 2016, *ApJ*, 833, 145
- Suzuki, D., Udalski, A., Sumi, T., et al. 2014, *ApJ*, 780, 123
- Suzuki, D., Udalski, A., Sumi, T., et al. 2014e, *ApJ*, 788, 97
- Szymański, M. K., Udalski, A., Soszyński, I., et al. 2011, *Acta Astron.*, 61, 83
- Tsapras, Y., Choi, J.-Y., Street, R. A., et al. 2014, *ApJ*, 782, 48
- Udalski, A., Jaroszyński, M., Paczyński, B., et al. 2005, *ApJ*, 628, L109
- Yelda, S., Lu, J. R., Ghez, A. M., et al. 2010, *ApJ*, 725, 331
- Zang, W., Hwang, K.-H., Kim, H.-W., et al. 2018, *AJ*, 156, 236